A groovy laser processing route to achieving high power and energy lithium-ion batteries

Pengcheng Zhu [a,b,j,*], Adam Boyce [c,j], Sohrab R. Daemi [d,j], Bo Dong [a,j], Yongxiu Chen [b,j], Shaoliang Guan [e,f,g], Mickey Crozier [h], Yu-Lung Chiu [b], Alison J. Davenport [b], Rhodri Jervis [d,j], Paul Shearing [d,i,j], Reza N. Esfahani [h,*], Peter R. Slater [a,j,*], Emma Kendrick [b,j,*]

[a] School of Chemistry, The University of Birmingham, Birmingham, UK
[b] School of Metallurgy and Materials, The University of Birmingham, Elms Rd, Birmingham B15 2SE, UK
[c] School of Mechanical and Materials Engineering, University College Dublin, Dublin 4, Ireland
[d] Electrochemical Innovation Lab, Department of Chemical Engineering, University College London, London, WC1E 7JE UK
[e] School of Chemistry, Cardiff University, Cardiff CF10 3AT, United Kingdom
[f] HarwellXPS, Research Complex at Harwell, Rutherford Appleton Laboratory, Didcot OX11 0FA, United Kingdom
[g] Maxwell Centre, Cavendish Laboratory, University of Cambridge, Cambridge, CB3 0HE, United Kingdom
[h] The Manufacturing Technology Centre Ltd, Coventry CV7 9JU, United Kingdom
[i] Department of Engineering Science, University of Oxford, Parks Road, Oxford OX1 3PJ, United Kingdom
[j] The Faraday Institution, Quad One, Harwell Campus, Didcot OX11 0RA, UK

ARTICLE INFO

ABSTRACT

3D-structured NMC622 with precisely controlled electrolyte channels were manufactured by incorporating femtosecond laser processing with conventional slurry casting. Demonstrated in a full cell for the first time, the 3D electrode structures mitigate plating and dendrite growth at the graphite electrode and lead to improved cycling performance, 75 % capacity retention vs 58 % after 500 cycles. 3D-structured NMC622 with a high areal capacity, 5.5 mAh cm^{-2}, exhibits an areal capacity retention of ~70 % and volumetric capacity exceeding 250 mAh cm^{-3} at ~1.15C, three times and twice that of a conventional slurry-casted NMC622, respectively. The improved rate performance is attributed to the enhanced ionic transport and reduced charge transfer resistance facilitated by the 3D electrode structure, as shown through galvanostatic titration measurements. A finite element method-based 3D model illustrated the improved uniform distribution of Li-ion concentration and state of charge within the 3D-structured electrode. Additionally, the 3D electrode structure proved beneficial for wettability and accelerated electrolyte absorption, leading to improved manufacturing efficiency.

1. Introduction

Lithium-ion batteries (LIBs) nowadays are ubiquitous energy storage devices and are widely adopted in portable electronic devices, electric transportation and even grid-scale energy storage [1]. LIBs play a pivotal role in advancing electrification and achieving our Net Zero goal by 2050 [2,3]. However, the energy and power densities of LIBs are yet to fully meet our demands. The limited driving range and slow charging speed of current electric vehicles are two exemplary bottlenecks for LIBs, making it difficult to completely displace conventional internal combustion engine vehicles in the short term [4]. Besides, LIBs are facing challenges in satisfying the needs of heavy-duty applications, such as

trucks, trains and aircraft [5–7]. These concerns necessitate further advancement in the energy and power performance of LIBs.

Electrodes are vital components in LIBs and have been extensively researched to improve LIB performance [8]. Previous research on electrodes can be generally categorized into two main areas: material discovery and structure optimisation. Electrode material discovery refers to identifying new electrode materials with higher capacity, higher operating voltage (cathode), faster Li-ion transfer kinetics, better electrical conductivity, higher stability and lower cost [9,10]. For example, utilising oxide anodes can significantly enhance power densities, while the lower voltage of such cells reduces the energy density, illustrating that this high energy and power target cannot easily be achieved through

electrode material substitution [11,12]. Electrode structure optimisation involves tuning electrode structures, such as porosity, pore size, pore distribution, to improve LIB performance, which has attracted more and more attention recently [13–16]. Current LIB electrodes have been manufactured using slurry casting for three decades since the first LIB was commercialised by Sony in 1991. Despite some advantages of cost-effectiveness and the ability to scale up, the limitation of slurry casting is also very obvious. Slurry casting has low controllability on the produced electrode structure and all slurry-casted electrodes have randomly distributed porosities, resulting in sluggish ionic transport [17]. As the electrode has been fabricated thicker and thicker to achieve higher energy densities, the ionic transport within the slurry-casted electrode can be further hindered due to the elongated transport pathway, resulting in unsatisfactory power density [18]. Besides, the energy density can be significantly reduced when the electrode thickness is over a critical value due to increased cell polarisation and underutilisation of active materials [19]. Li et al. pointed out the requirement for low-tortuosity electrodes for simultaneous high-energy and high-power batteries [20].

Achieving high energy and high power concurrently with conventional slurry-casted electrodes has been proven to be very challenging. To this end, much effort has been made to manufacture electrodes with specific structures while allowing high thickness and fast ionic transport, such as via various templating routes [21–25], additive manufacturing [26–29], laser processing [30,31] and multilayer coating [32,33]. As discussed in a recent comprehension review on electrode processing, the main considerations on these processes are around scalability, throughput and cost [34]. Among them, laser processing provides a facile and effective route to fabricate structured electrodes with highly controlled electrode geometry and structures. Furthermore, laser processing shows high compatibility with the existing slurry casting process, making it a promising avenue for future electrode manufacturing. Pfleging systematically summarised research advances in laser electrode processing [35]. Various cathodes and anodes, including graphite [36], carbon-coated silicon [37], silicon/graphite composite [38], lithium nickel manganese cobalt oxide (NMC) [39], have been successfully processed by laser and demonstrated improved performance, e.g. electrolyte wettability, improved ionic transport and rate capability. However, many questions remain unclear. In particular, studies have been limited to half-cell configurations, so the impact of electrode structural modification on the counter electrode in a full-cell design is still unknown. Furthermore, the distributions of the state-of-lithiation and lithium-ion concentration within the laser-created 3D electrode structure have not been well studied. Although laser-induced breakdown spectroscopy has been proven to be a functional technique to map lithium-ion distribution, most studies are limited by 2D structure characterisations and the resolution needs further improvements [40,41]. Furthermore, optimal structures and potential side effects of laser processing are also factors that need to be systematically studied. Addressing these concerns will be crucial for achieving the full promise of laser processing.

In this work, we utilised the femtosecond laser technique to create 3D structures on a standard cathode, NMC622, aiming to improve the power density. The influence of a structured cathode on the counter electrode in a full cell was investigated for the first time. Moreover, all NMC 622 electrodes have high mass loadings of up to 38 mg cm^{-2} and corresponding areal capacities over 6 mAh cm^{-2} before laser processing, giving rise to high energy densities. The laser-created structure and associated morphology change were observed by scanning electron microscope (SEM) and micro X-ray computed tomography (micro CT) and optical microscope. Possible chemical composition change was characterised by energy dispersive spectroscopy (EDS) and X-ray photoelectron spectroscopy (XPS). The electrolyte absorption performance, ionic transport in electrolyte within the electrode, charge transfer resistance, and Li-ion diffusion in the solid state were investigated. The improvement in 3D structure in Li-ion transport was further

illustrated and understood using finite element method-based electrochemical modelling. This work provides a comprehensive understanding of the 3D laser-structured electrodes with a view to paving the way for future wide adoption of laser technique in electrode manufacturing for high-performing Li-ion batteries.

2. Results and discussion

NMC622 electrodes were first fabricated by conventional slurry casting and then transferred to a laser machine for processing, as illustrated in Fig. 1a. Femtosecond pulsed laser beams were directed onto the electrode to selectively remove materials at certain locations to create specific structures. Figs. 1b and c show the micro-CT scanned images of the cross-section of NMC622 electrodes before and after processing, respectively. Some grooves created by laser beams are visible in Fig. 1c. All laser-created grooves have a tapered cross-section due to the interaction between laser beams and the electrode material and associated energy loss as the laser beam goes deeper into the electrode [30]. Figs. 1d and e show the top view of the NMC622 electrodes before and after processing. The laser-created grooves are straight channels from the top angle and parallel to each other. Two parameters of the laser-structured NMC622 were defined in Figs. 1f and g: groove size and plateau size. The groove size is defined as the top width of the straight channel, and the plateau size is the distance between two adjacent channels. A 3D optical microscopy image of the laser-structured electrode is shown in Figure S1.

Fig. 2a shows the laser-created structures with three different groove sizes of 70, 110, 210 μm (left to right) and three different plateau sizes of 100, 200, 400 μm (top to down). Both the groove and plateau sizes can be controlled by controlling the laser parameters. The smallest achievable groove size is about 50 μm due to the resolution of the setup (F-Theta F160mm focal length lens). Information on electrode porosity, areal capacity and structural parameters of all samples is shown in Table 1. Fig. 2b shows the electrolyte absorption performance of the laser-structured electrode with a groove size of 70 μm and a plateau size of 100 μm (sample 1) and an unstructured electrode. The vertical axis is the time from 0 to 1 s. As an electrolyte droplet dropped on the top of the two electrodes, the laser-structured electrode can completely absorb the electrolyte in about 0.5 s, while the unstructured electrode still has electrolyte on the top after 1 s, demonstrating that the laser-structured electrode has faster electrolyte absorption. It should be noted that the electrolyte droplet was dropped randomly on the surface of the electrodes and the diameter of the electrolyte droplet is about 1.8 mm, much bigger than all laser-created grooves. The electrolyte absorption speed mainly depends on the surface tension of the electrolyte and the surface free energy of the electrodes, as previously reported in [42]. For this study, a consistent electrolyte was utilised across all experiments, ensuring uniformity in electrolyte properties. The observed enhancement in electrolyte absorption speed can be therefore attributed to the increased effective capillary radius and increased electrode porosity [43, 44]. Similar results can be seen for other laser-structured electrodes in Figure S2. The improved electrolyte absorption performance of the laser-structured electrodes has practical significance to industries as it can shorten the soaking time required and thus improve cell manufacturing efficiency.

Figs. 3a-c show the side wall of the laser-created grooves (laser-irradiated area) at different magnifications. The surface morphology of the side wall has been significantly changed after laser processing. In Fig. 3b, secondary particles are clearly visible on the top of the electrode (pristine area), while the laser-irradiated area shows a much flatter surface without any secondary particles. At a higher magnification in Fig. 3c, the laser-irradiated area shows a very rough surface with large sub-micron-sized particles which are very likely the primary particles. Besides, some micron-sized cracks can be observed, which might be formed by laser-induced stress and can benefit electrolyte penetration and Li-ion transport. Fig. 3d shows the cross-section of a single groove
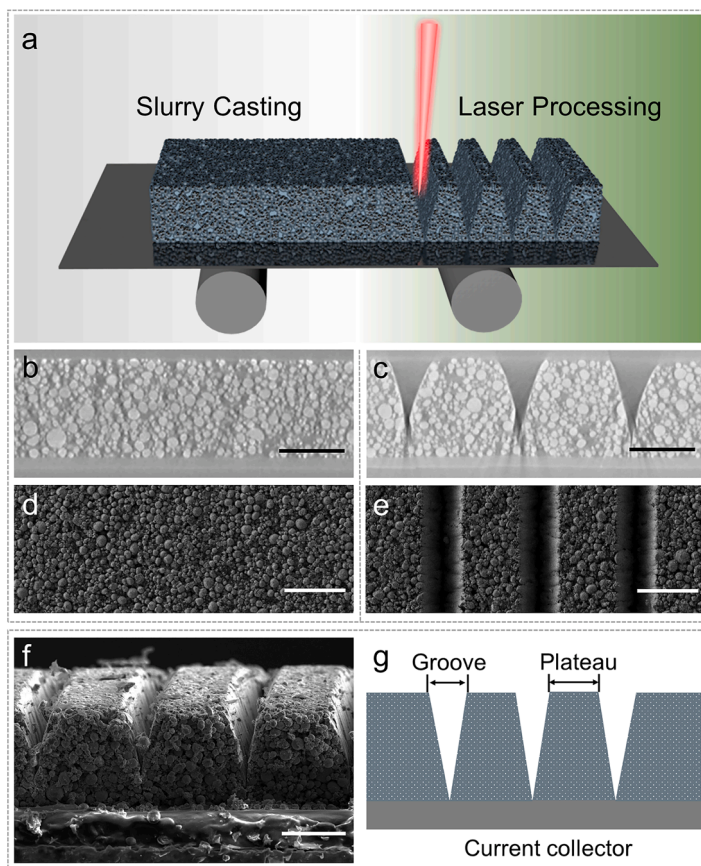
Fig. 1. NMC622 before and after laser processing. **a)** Schematic illustration of NMC622 after slurry casting and laser processing, micro-CT scanning images of the cross-section of NMC622 **b)** before and **c)** after laser processing, SEM images of the top view of NMC622 **d)** before and **e)** after laser processing, **f)** SEM image and **g)** schematic illustration of the cross-section of a laser-structured NMC622 (scale bar: 100 μm).
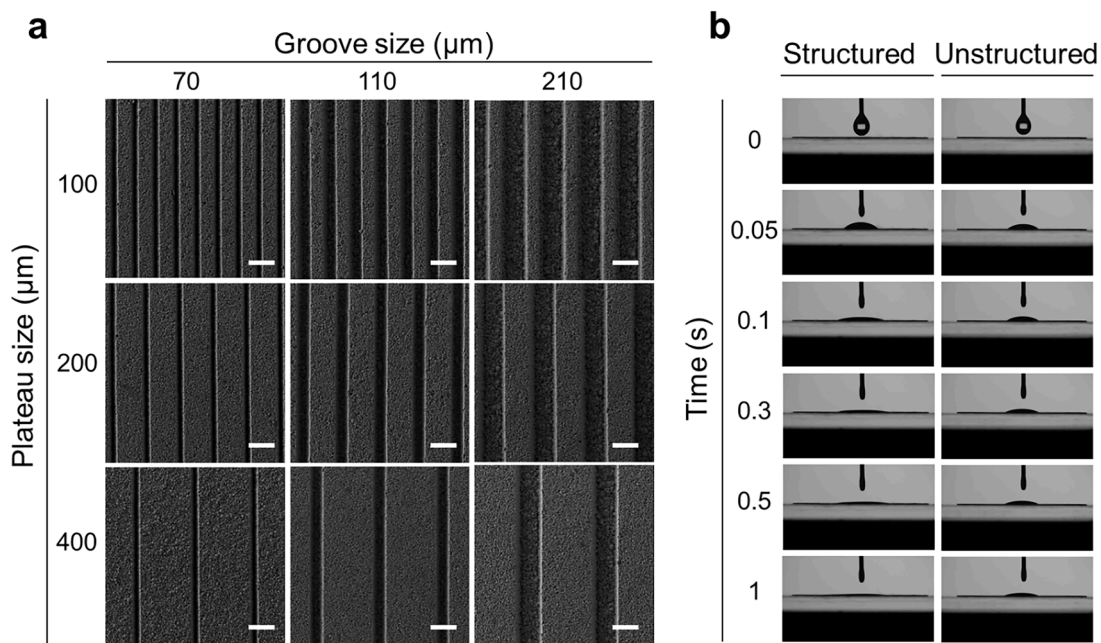
Fig. 2. Laser-created structures and electrolyte absorption performance. **a)** laser-created structures with three different groove sizes of 70, 110 and 210 μm (left to right) and three different plateau sizes of 100, 200 and 400 μm (top to down), **b)** electrolyte absorption on the top a laser-structured electrode (groove size: 70 μm & plateau size: 100 μm) and an unstructured electrode. (scale bar: 200 μm).

Table 1
Sample information.

|	Groove size (μm)	Plateau size (μm)	Porosity	Density (g cm^{-3})	Areal capacity (mAh cm^{-2})
1	70	100	49.46	2.34	5.05
2	70	200	46.21	2.49	5.47
3	70	400	44.28	2.58	5.33
4	110	100	61.69	1.77	3.49
5	110	200	53.21	2.16	4.33
6	110	400	47.57	2.42	5.50
7	210	100	69.52	1.41	2.86
8	210	200	63.03	1.71	3.74
9	210	400	54.22	2.12	4.80
10	Unstructured		41.62	2.70	6.05

and Fig. 3h is the selected area for EDS mapping. It is clear to see that a thin layer of a few microns is formed on the side wall of the groove in Fig. 3h. EDS mapping further illustrates the carbon content is much lower in the thin surface layer compared with the bulk electrode (Fig. 3e). Considering laser processing can cause localised heat accumulation, the carbon near the surface is likely to be burnt out, resulting in reduced carbon content. Other elements seem not to be affected too much by laser processing from the EDS maps (Figs. 3f, g, i, j, k). XPS spectra show the surface composition of the pristine and laser-irradiated areas. The survey scan spectra can be seen in Figure S3. It is clear to see that the atomic percentages of carbon and fluorine contents are reduced from 63.33 to 57.39 (Fig. 3l) and 18.36 to 8.51 (Fig. 3m) after laser processing, respectively, while the oxygen percentage shows a significant increase from 10.63 % to 25.83 % (Fig. 3n). The increased oxygen content mainly comes from the enhanced surface oxygen peak at about 532 eV, which can be attributed to the oxidation at the surface induced by high-energy laser beams and the partial removal of conductive carbon and PVDF binder [31]. In Fig. 3l, a small peak at ~283 eV is increased after laser structuring, which is indicative of the formation of a trace amount of carbides, e.g. nickel carbide [45]. The peak at about 685 eV in Fig. 3m corresponding to LiF shows an increase after laser processing [46,47]. There are no obvious differences in the XPS spectra of the transition metal elements, Ni, Mn and Co (Figure S3) before and after laser processing.

Figs. 4a and b show the cyclic voltammogram of a laser-structured and an unstructured NMC622 for a potential range of 2.5–4.25 V and
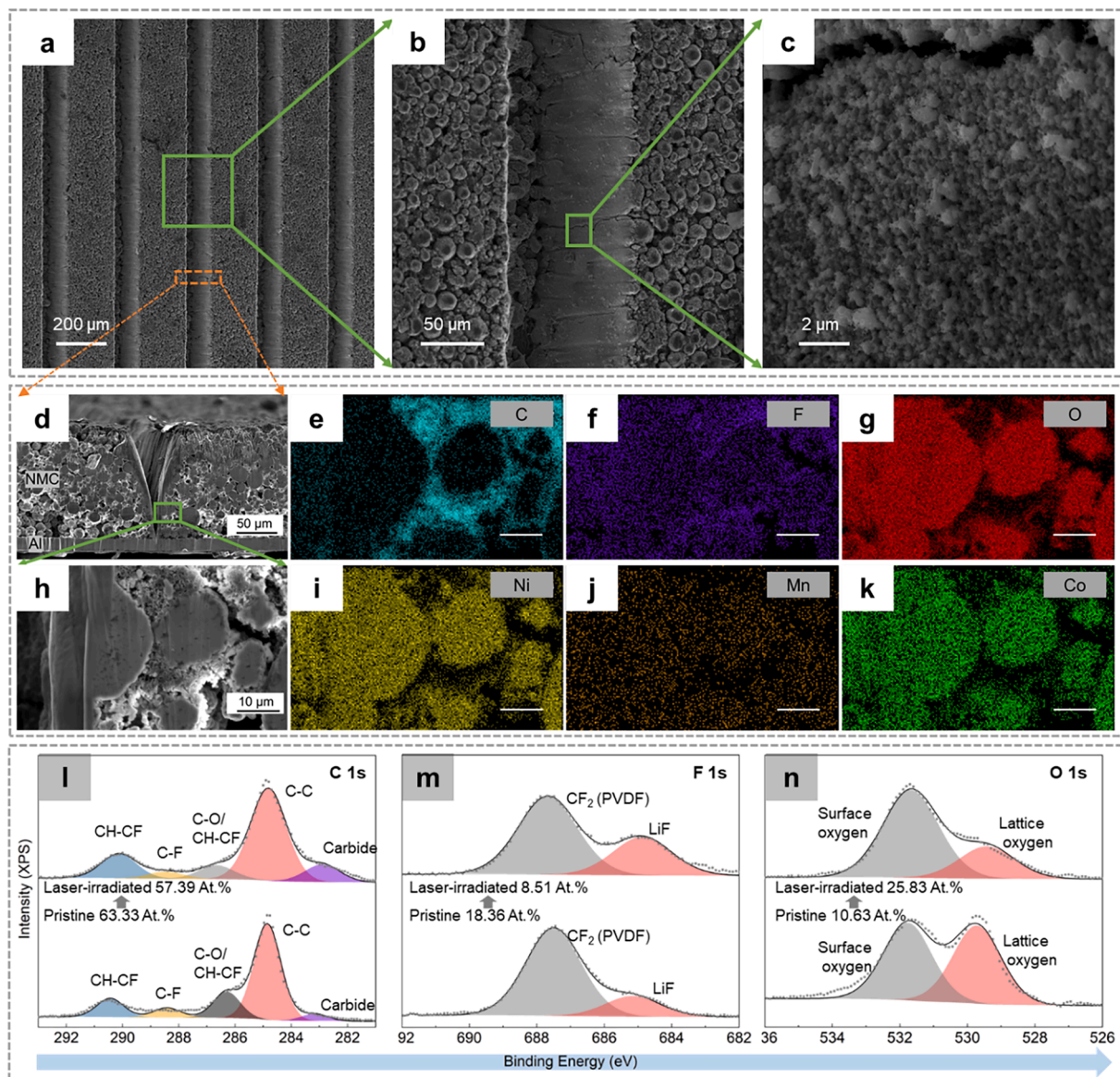
Fig. 3. Surface morphology and composition of before and after laser processing. **a)-c)** surface morphology of laser-irradiated area at different magnifications, **d)-k)** EDS mapping in the selected area **h)**, **l)-n)** XPS spectra of different elements in the laser-irradiated area.
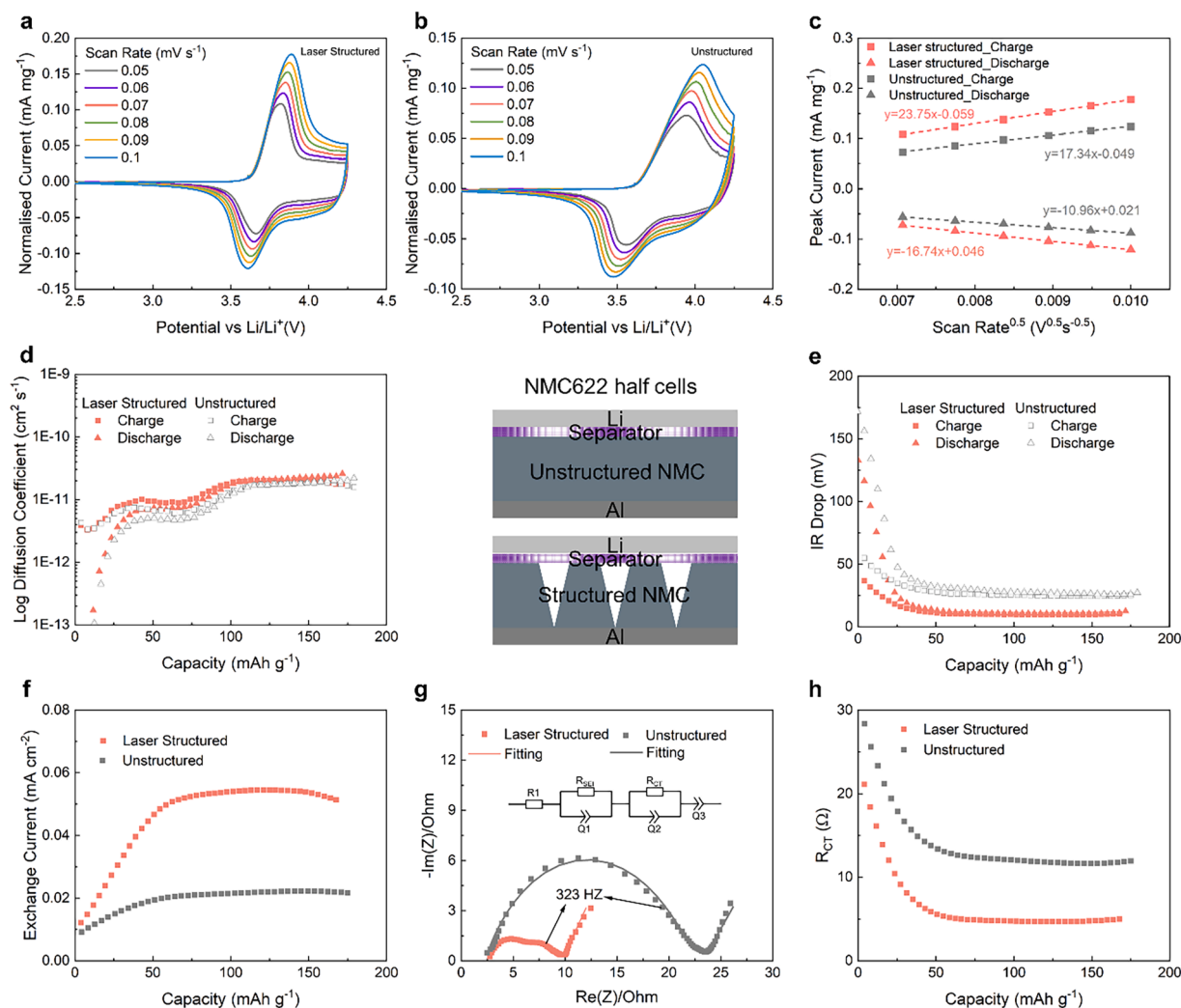
Fig. 4. Electrochemical characterisation of laser-structured (sample 1, groove: 70 μm & plateau: 100 μm) and unstructured electrodes in half cells. **a-c:** cyclic voltammogram of **a)** laser-structured and **b)** unstructured electrodes, **c)** correlation between peak current and square root of scan rate, d-f: GITT measurements for **d)** solid-state Li-ion diffusion coefficient, **e)** IR drop, **f)** exchange current density, **g)** EIS plots measured at 50 % SOC, **h)** charge transfer resistance.

different scan rates of 0.05–0.1 mV s^{-1}. The laser-structured electrode has a groove size of 70 μm and a plateau size of 100 μm (sample 1). Considering that the two electrodes have slightly different mass loadings, the current is normalised with the weight of the active material. The anodic and cathodic peaks in the two voltammograms are at similar potentials, suggesting identical redox reactions for both laser-structured and unstructured NMC622. Moreover, the unstructured NMC622 exhibits a more pronounced distortion with the anodic peak shifting right and cathodic peak shifting left in its voltammogram compared to the laser-structured counterpart, indicating higher polarization, which is related to slow mass transport. Fig. 4c plots the anodic and cathodic peak currents against the root square of the scan rate. The peak currents are proportional to the square root of the scan rate, implying that the redox reactions are diffusion-controlled [48]. According to the Randles–Sevcik equation, the diffusion coefficient is proportional to the peak current divided by the square root of the scan rate, i.e. the slopes of the linear fitting lines [49]. The slopes are 23.75 and 16.74 in charging and discharging cycles for the laser-structured electrodes, higher than the unstructured electrode (17.34 and 10.96), demonstrating that the laser-structured electrode has a faster Li-ion diffusion than the unstructured one. It should be noted that the Li-ion diffusion mentioned here includes Li-ion transport in the electrolyte-filled pores (liquid-state diffusion) and the Li-ion diffusion in active material particles (solid-state diffusion) [50]. Figure S4e plots the anodic peak currents against the

scan rate and further fits the plots using the power law equation $y = ax^b$. The b values for the laser-structured and unstructured electrodes are 0.71 and 0.74, respectively, implying similar charge storage processes and likely mixed reaction control mechanism by both the electrode surface ($b = 1$) and Li-ion diffusion ($b = 0.5$) in the selected scan rate range [48,51]. The laser-structured electrode shows a higher a value of 0.92 than the unstructured one (0.68), which is likely due to increased electrode surface and enhanced electrode/electrolyte contact after laser processing.

The apparent diffusion coefficient of Li-ions in the solid state is measured by the galvanostatic intermittent titration technique (GITT) and shown in Fig. 4d. The measured diffusion coefficient mainly ranges from 10^{-12} to 2×10^{-11}, which is consistent with previous studies [52, 53]. The laser-structured electrode exhibits a solid-state Li-ion diffusion coefficient that is very close to and marginally higher than the unstructured electrode, suggesting that laser structuring has a minimal impact on the solid-state diffusion of Li-ions. As reported previously in [52,54], the Li-ion diffusion coefficient measured by GITT is not solely determined by the solid-state diffusion but is also influenced by the Li$^+$ transport within the electrolyte at high electrode thicknesses. The slight improvement in solid-state Li-ion diffusion from the laser-structured electrode may result from the enhanced ionic transport within the electrolyte.

Fig. 4e shows that the laser-structured electrode exhibits lower IR

drops than the unstructured electrode. The raw GITT plots for the laser-structured and unstructured electrodes can be seen in Figure S4. The IR drop is the sum of an ohmic overpotential (η_{ohm}) and a charge-transfer overpotential (η_{CT}) [55]. The ohmic overpotential can be calculated by multiplying the series resistance(R_S) with applied current density (I), as shown the Equation:

$$IR\ drop = \eta_{ohm} + \eta_{CT} = IR_s + \eta_{CT}$$

Considering the series resistances are around 2.5 Ω (EIS measurement in Fig. 4g) and the applied currents are similar for both the laser-structured and unstructured electrodes, the lower IR drop of the laser-

structured electrode implies smaller charge transfer overpotential and faster reaction kinetics. The higher exchange current density of the laser-structured electrode in Fig. 4f further confirms the faster reaction kinetics. The charge transfer resistance can be obtained through electrochemical impedance measurement (EIS) in Fig. 4g. At an identical SOC of 50 %, the laser-structured electrode shows smaller semicircles than the unstructured electrode, indicating a smaller internal resistance [56]. By fitting the Nyquist plots with the equivalent circuit inserted in Fig. 4g [57], the laser-structured electrode shows a charge transfer resistance (R_{CT}) of 6.1 Ω, about one-third of the unstructured electrode (19.3 Ω). GITT measurement gives slightly lower values for R_{CT}, 4.9 Ω and 12.3 Ω
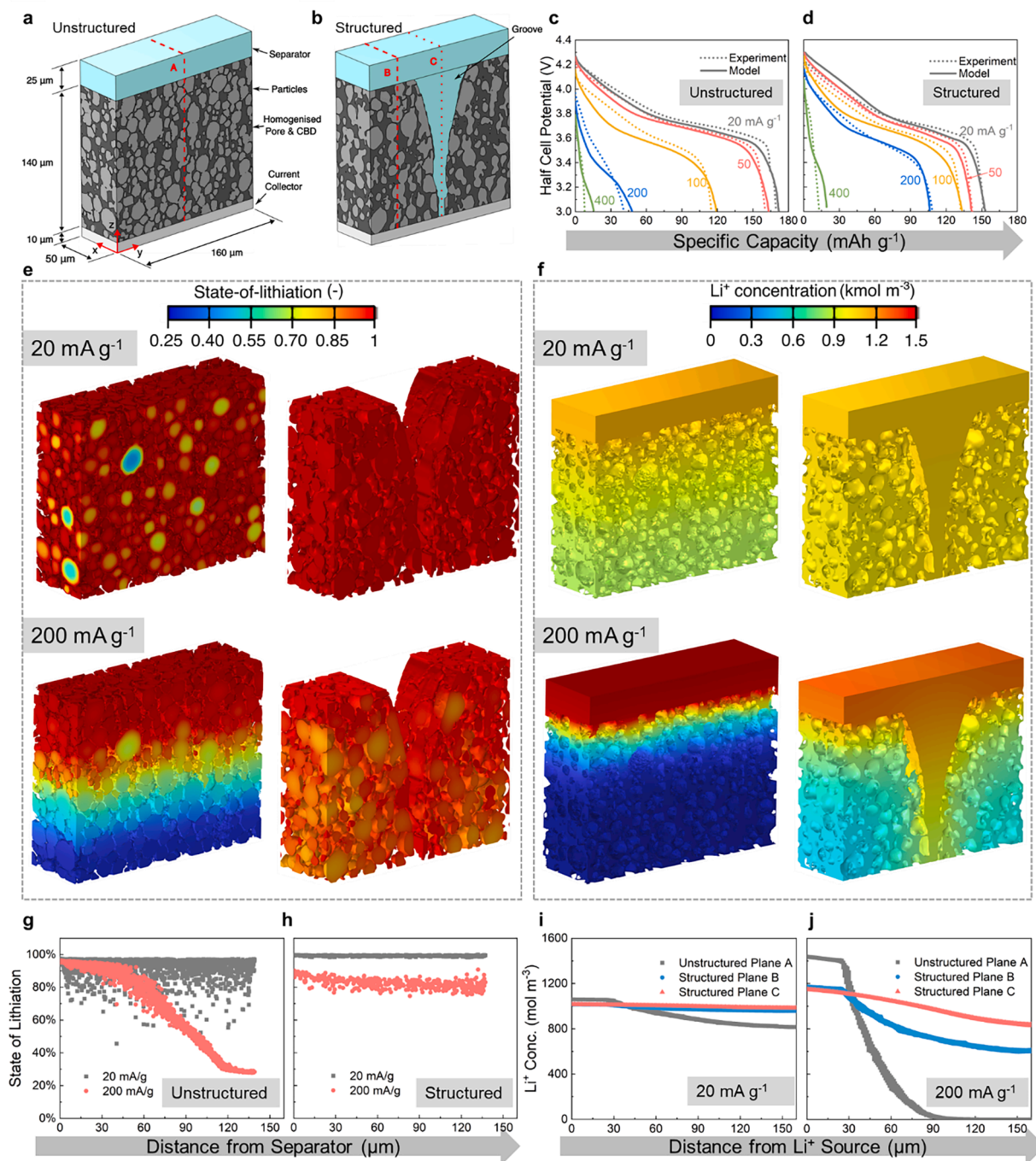
Fig. 5. 3D structure reconstruction and electrochemical modelling. Electrode geometry for **a)** unstructured and **b)** structured models. Half cell discharging plots for **c)** unstructured and **d)** the structured NMC622 at different current densities from 20 to 400 mA g^{-1}. **e)** State-of-lithiation in particles and **f)** lithium-ion concentration profiles within the electrolyte and porous regions at the end of 20 and 200 mA g^{-1} discharge. Quantitative distribution of **g)-h)** SOC and **i)-j)** lithium-ion concentration along the direction of electrode thickness.

for the laser-structured and unstructured NMC622 in Fig. 4h, respectively. Both the EIS and GITT measurements show a lower charge transfer resistance from the laser-structured electrode. This can be ascribed to the increased contact area between the electrode active materials and the electrolyte after the laser processing. All of the EIS fitting parameters are shown in Table S1. It is worth mentioning that the ohmic resistance of the laser-structured and unstructured electrodes are very similar, around 2.5 Ω, suggesting that the laser structuring has a negligible effect on the overall electrical conductivity of the electrode and current collector [58]. The diffusion coefficient, exchange current density and open circuit voltage (Figure S4c) measured by the GITT test were fed into an electrochemical model to investigate the quantitative impact of the laser-structured electrode on the distributions of Li-ion concentration and state of charge/discharge.

Finite element method-based electrochemical modelling was used in this study for both unstructured and laser-structured electrodes [59,60]. The models were based on the 3D structures reconstructed from micro-CT scanned images, as shown in Figs. 5a and b. The models were parametrised using the diffusion coefficient and exchange current density as outlined in Fig. 4 as well as the open-circuit potential in Figure S4c, which enables the models to have a strong underlying experimental foundation. Figs. 5c and d display the discharge plots of the unstructured and laser-structured NMC622 at different current densities from 20 to 400 mA g^{-1}. It is clear that the modelling and experimental results are in good agreement. Figs. 5e and f further illustrate the state-of-lithiation (SOC) and Li$^+$ concentration profiles within the electrodes at the end of the discharge, respectively. The SOC is defined as the ratio of the instantaneous lithium concentration at a given point in the domain and the maximum possible lithium concentration. At a low current density of 20 mA g^{-1}, both laser-structured and unstructured NMC622 show a relatively uniform distribution of SOC and Li$^+$ concentration. At a high current density of 200 mA g^{-1}, the laser-structured NMC622 exhibits much more uniform distributions of the SOC and Li$^+$ concentration, while the unstructured NMC622 shows

severe gradients in the SOC and Li$^+$ concentration along the direction of electrode thickness. Figs. 5g and h further show the quantitative SOC gradient. The SOC is defined as the SOC at the centre of each active material particle. At the end of 200 mA g^{-1} discharge, the laser-structured NMC622 shows a uniform SOC distribution between 70−100 %, while the unstructured NMC622 exhibits a much wider range, with ~100 % SOC at the surface close to the separator and only ~20 % SOC at the surface close to the current collector. Figs. 5i and j plot the Li$^+$ concentration within the electrolyte and porous regions along three planes (A in the unstructured NMC622, B and C in the structured NMC622) identified in Figs. 5a and b. At 20 mA g^{-1}, the Li$^+$ concentration is high and uniformly distributed along all three planes. A severe Li$^+$ concentration gradient can be seen in the unstructured NMC622 (plane A) as the discharge current is increased to 200 mA g^{-1}, with complete Li$^+$ depletion occurring within a large portion of the electrode. On the contrary, the laser-structured NMC622 (planes B and C) shows much smaller gradients, indicating enough Li$^+$ distribution throughout the electrode. The models provide direct visualisation of the state-of-lithiation and Li$^+$ concentration, which confirms that laser-created grooves are beneficial for Li-ion transport and electrode performance.

Fig. 6a shows the gravimetric capacity of all NMC622 electrodes studied in this work. At current densities higher than 100 mA g^{-1}, all laser-structured NMC622 deliver remarkably higher gravimetric capacities than the unstructured one. The improved rate performance is attributed to the enhanced Li-ion transport and reduced charge transfer resistance. Nevertheless, all laser-structured NMC622 electrodes exhibit slightly lower capacities than the unstructured one at lower current densities of 10–50 mA g^{-1}, which is very likely due to the surface change after laser processing. The laser-irradiated area has reduced carbon content and therefore lower electrical conductivity and reduced capacity. Fig. 6b compares the rate performance of the laser-structured NMC622 with an identical groove size of 110 μm and three different plateau sizes of 100, 200 and 400 μm. At current densities < 100 mA g^{-1},
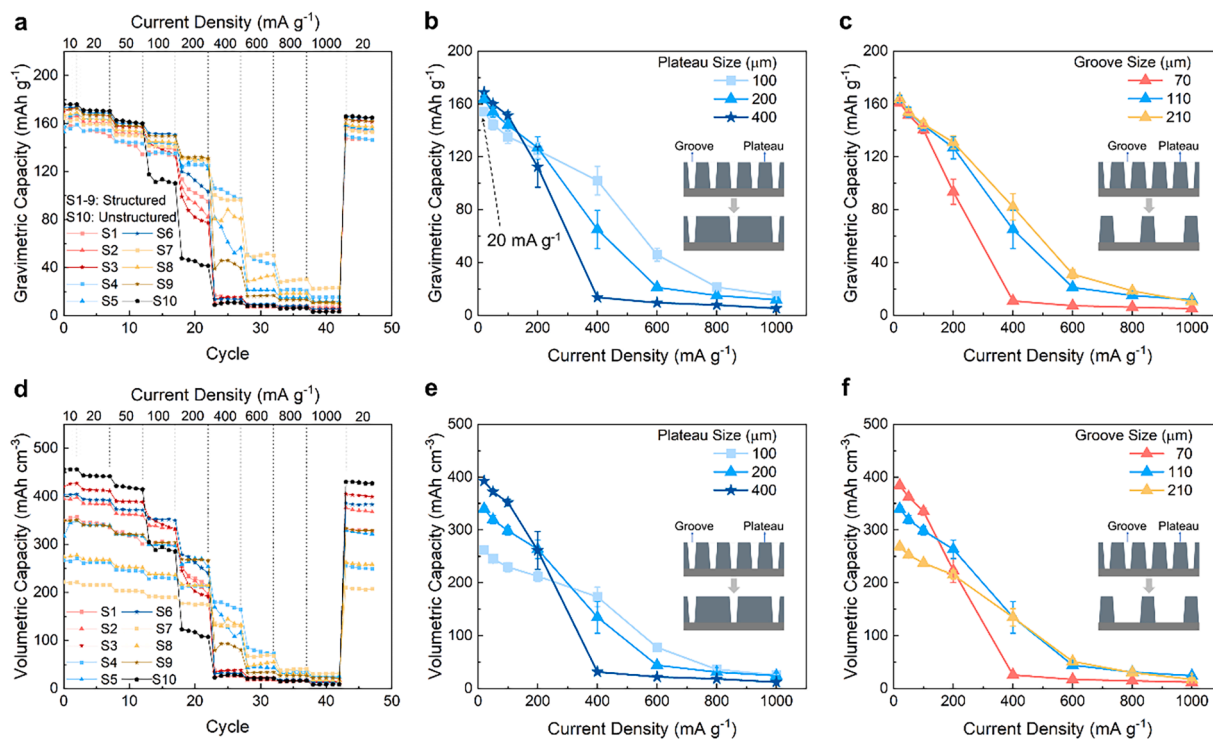

Fig. 6. Battery testing results (Samples 1–9: laser structured NMC622, Sample 10: unstructured NMC622). gravimetric capacity of **a)** all NMC622 electrodes, **b)** laser-structured NMC622 with an identical groove size of 110 μm, **c)** laser-structured NMC622 with an identical plateau size of 200 μm; volumetric capacity of **d)** all NMC622 electrodes, **e)** laser-structured NMC622 with an identical groove size of 110 μm and **f)** laser-structured NMC622 with an identical plateau size of 200 μm.

a larger plateau size results in a higher capacity, implying that capacity increases as the number of laser-created grooves decreases. This supports our interpretation of capacity loss, that is, the more grooves are made, the more capacity will be lost at low current densities. At a high current density of 400 mA g^{-1}, the laser-structured NMC622 with a smaller plateau size delivers a higher capacity, which can be explained by better Li-ion transport and smaller charge transfer resistance when more grooves are created. Similar results can be seen from the other two groups of samples with groove sizes of 70 and 210 μm in Figures S5a and b. Fig. 6c plots the capacity of the laser-structured NMC622 with an identical plateau size of 200 μm and three different groove sizes of 70, 110 and 210 μm. A larger groove leads to higher capacities regardless of the current density, suggesting that larger grooves facilitate Li-ion transport better. Laser-structured NMC622 electrodes with different plateau sizes of 100 and 400 μm follow the same trend (Figures S5c and d). It should be noted that the laser-structured NMC622 with a groove/plateau size of 110/400 μm (Sample 6) has an areal capacity of 5.5 mAh cm^{-2} and can show capacity retention of up to 70% at a current density of 200 mA g^{-1} (~ 1.15C), about three times of the unstructured electrode (26 %, as shown in Figure S6), showing the potential of achieving high energy and power concurrently.

Volumetric capacity is another important parameter that needs to be considered, particularly in compact devices whose volume is strictly limited. The volumetric capacity is defined as the capacity per unit volume of the electrode and calculated by equation [61]:

$$Volumetric\ capacity = Gravimetric\ capacity * electrode\ density$$
$$* active\ material\ ratio$$

The electrode density can be found in Table 1 and the active material ratio is 96 %. Fig. 6d illustrates that all the laser-structured NMC622 deliver lower volumetric capacities than the unstructured one at 10–50 mA g^{-1}, which can be ascribed to the increased porosity and capacity loss caused by surface change after laser structuring. At a current density of 100 mA g^{-1} or higher, structured electrodes start to surpass the unstructured one in the volumetric capacity as the Li-ion transport becomes a limiting factor at high current densities and laser-created structures are beneficial for Li-ion transport. Figs. 6e and f show that a large plateau or a small groove leads to higher capacities at low current densities because of fewer grooves created and therefore lower electrode porosities and less capacity loss. On the contrary, a small plateau or large groove is beneficial at high current densities due to better Li-ion transport and mass transfer. Similar results can be seen in Figure S7. Structured NMC622 with groove/plateau size of 110/400 (Sample 6) delivers

only about 10 % lower volumetric capacity than the unstructured one at 20 mA g^{-1} but more than twice the volumetric capacity at 200 mA g^{-1} (~1.15C), showing great potential for the application in compact devices.

The effect of laser-created structures on electrode performance can be understood through porosity. Electrodes subjected to different laser processes exhibit distinct porosities (Table 1). Figure S8 shows the effects of electrode porosity on gravimetric and volumetric capacities. Gravimetric capacity slightly decreases with increasing porosity at a low current density of 20 mA g^{-1} due to more grooves created and more surface changes generated, while at a high current density of 200 mA g^{-1}, gravimetric capacity increases with increasing porosity due to enhanced Li-ion transport. Additionally, volumetric capacity decreases with increasing porosity at a low current density of 20 mA g^{-1} due to less electrode density. At a high current density of 200 mA g^{-1}, volumetric capacity initially increases but subsequently decreases with increasing porosity due to the combined effects of material loss and enhanced Li-ion transport. The optimal porosity is around 50 %, similar to the identified optimal structure (sample 6).

Fig. 7a shows the cycling performance of NMC/graphite full cells at 100 mA g^{-1}. The full cell with a laser-structured NMC622 (Sample 1: 70 μm grooves and 100 μm plateaus) shows a better cycling performance, with ~75 % capacity retention after 500 cycles. For comparison, the full cell with an unstructured NMC622 only shows a capacity retention of around 58 %. The cycling performance can be explained by lithium metal deposition formed on the graphite electrode, as shown in the inserts in Fig. 7b. The two circular electrodes were obtained by disassembling the full cells after 500 cycles. The light region on the two circle electrodes is lithium metal deposition and the dark region is graphite, as evidenced by SEM images at the bottom. It is obvious that the graphite anode working against the laser-structured NMC622 shows less coverage of lithium deposition. Besides, it is interesting to observe that the deposition shows a negative replica of the grooved structure of the laser-structured NMC622, ~100 μm-sized grooves between ~70 μm width of deposited lithium, suggesting that the laser-created structure on the cathode can limit lithium metal deposition at the anode. This indicates that the inhomogeneous current distribution on the cathode is reflected in the anode electrode, resulting in lithium deposition opposite to the cathode ridges.

Future efforts can focus on laser processing parameter optimisation, such as laser pulse frequency, pulse duration, scanning speed, etc. to minimise the laser-induced surface change and capacity loss. In addition, the introduction of an inert atmosphere during the processing is
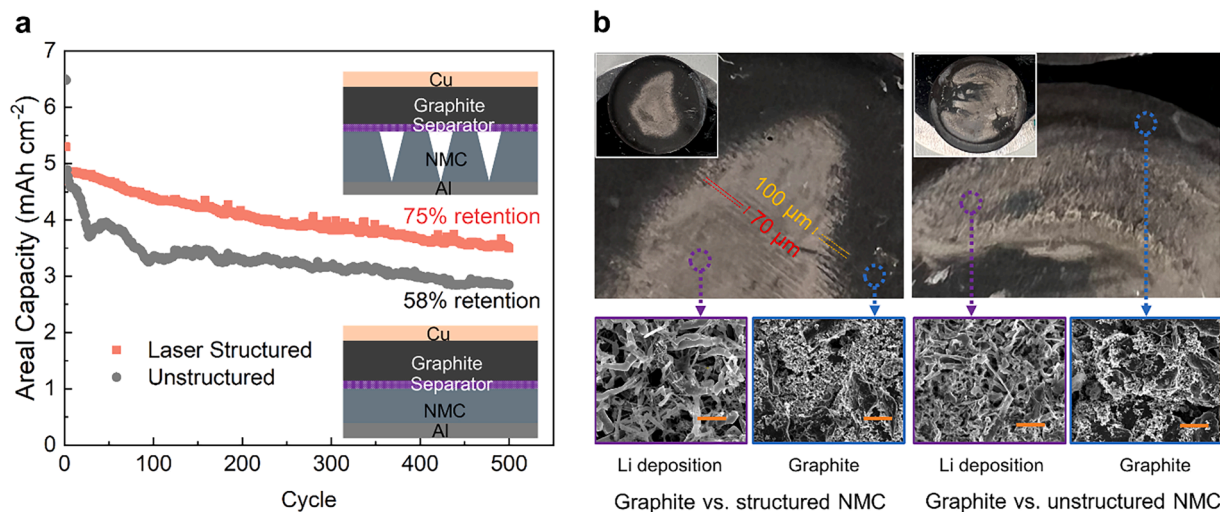

Fig. 7. Cycling and post-mortem analysis. **a)** cycling performance of NMC622/Graphite full cells at 100 mA g^{-1}, **b)** surface morphology of graphite anodes after 500 cycles. (scale bar: 10 μm).

also expected to be beneficial. In this work, it can take up to 10 h to process one piece of NMC622 with dimensions of ca. 10×20 cm^2 using the femtosecond laser and the associated capital cost is high. Further optimisation should also aim to significantly shorten the processing time required and lower the cost, for example, utilising cheaper nanosecond laser, while the greater thermal effect on electrode materials and processing precision need to be tested. Additionally, laser ablation inevitably increases the electrode porosity and the amount of electrolyte required, diminishing the energy density at the cell level. Despite the significant performance gains, future effort could leverage a larger database and machine learning techniques to optimise the laser-created structures further, aiming to use the electrode porosity more efficiently and enhance performance without necessarily increasing porosity infinitely.

3. Conclusions

In this work, we successfully fabricated highly controllable 3D structured NMC622 electrodes containing electrolyte channels, by applying femtosecond laser processing to high-loading slurry cast electrodes. Despite ablation of the cathode particles by the laser, which resulted in lower carbon content at the surface of the channels, high gravimetric and volumetric capacities are observed even at higher current rates, and when demonstrated in a full cell for the first time an improved capacity retention of 75 % was observed, compared to 58 % after 500 cycles due to improved electrolyte transport to the entire electrode thickness.

An interesting observation in the full cell, requiring further investigation is the impact of the structured cathode upon the graphite electrode. Despite improved cycle life, some lithium deposition was observed in stripes which reflect the electrode areal current density distribution in the cathode. This observation indicates that structuring the anode may also help to further improve cell rate and cycling performance.

The optimal structure identified in this work is a groove size of 110 μm and a plateau size of 400 μm (sample 6). This laser-structured NMC622 has a high areal capacity of 5.5 mAh cm^{-2} and an areal energy density over 200 Wh m^{-2} at the electrode level by assuming an average voltage of 3.7 V, almost double that of commercial lithium-ion battery electrodes [62]. At ~1.15C discharge, this laser-structure NMC622 can deliver up to 70 % capacity and a volumetric capacity over 250 mAh cm^{-3}, three times and twice that of a slurry-casted NMC622, respectively. This superior rate capability of the 3D-structured NMC622 is attributed to the enhanced lithium mass transport within the electrode. Significantly reduced tortuosity of the electrode is achieved with electrolyte channels which reach the current collector surface. This facilitates ion transport and results in a more homogeneous lithium distribution and hence improved charge transfer or current distribution across the thickness of the electrode. The improved mass transport and electrode reaction kinetics are shown by a voltage peak shift in the cyclic voltammetry and reduced charge transfer resistance and overpotential in EIS and GITT.

4. Experimental section

4.1. Initial electrode manufacturing

NMC622 electrodes were fabricated by slurry casting, with a formula of 96 wt% NMC622, 2 wt% polyvinylidene fluoride (PVDF) and 2 wt% C65. PVDF (Solvay) was pre-dissolved in NMP to make a PVDF solution with a concentration of 8 wt%. Half the 8 wt% PVDF solution was mixed with C65 powder (Imerys) using a THINKY mixer (ARE-20, Intertronics) at 500 rpm for 1 min and 2000 for 5 min. NMC622 powder (Targray) and the other half of the PVDF solution was added to the mixture and mixed again at 500 rpm for 1 min and 2000 rpm for 10 min. The mixture was subsequently degassed in the THINKY mixer at 2200 rpm for 3 min. The

obtained slurry was homogenous and had a solid content of around 60 %. The mixed slurries were then coated on Al current collectors with an areal capacity of around 6 mAh cm^{-2}. NMC622 coatings were initially dried at 80 °C to remove most solvents followed by overnight drying in a vacuum oven at 120 °C. The dried electrodes were calendered to porosities of around 40 %.

4.2. Laser processing

A Georg Fischer Machining Solutions Laser system (P 400 U - 5 Axis) and a femtosecond pulsed IR laser source (Pulse duration = 290 fs, Wavelength = 1032 nm) were used to create 3D structures in the slurry-casted NMC622. The laser parameters were set as: average power = 6 W, frequency = 500 KHz, scanning speed = 2000 mm/s, scan hatch distance = 0.02 mm. The laser-created grooves have three different top widths of 70, 110 and 210 μm and three different plateau sizes of 100, 200 and 400 μm, as illustrated in Fig. 2. Considering all slurry-cast NMC622 coatings have a thickness of ~140 μm, laser processing was repeated for 90 runs to create deep groves throughout the coating. Some debris settled on the electrode surface after laser processing and were subsequently removed by an air duster.

4.3. Scanning electrode microscopy with energy-dispersive X-ray (SEM-EDX) spectroscopy analysis

The surface morphology of the NMC622 before and after laser processing was investigated by scanning electron microscopy (Apreo 2 SEM) under an acceleration voltage of 10 kV. For the observation of the side wall of laser-created grooves, the sample stage was tilted to focus on the side wall. For cross-sectional observation, the cross-section of NMC622 electrodes was prepared by a broad ion beam system (ArBlade 5000, Hitachi). The elemental distributions were measured by the built-in energy-dispersive X-ray spectroscopy (EDX).

Cycled coin cells were decrimped and opened in a glovebox. Graphite anodes were washed with anhydrous dimethyl carbonate (DMC) and dried before being transferred to another glovebox connected to an SEM. The surface of the graphite anodes was then observed using a FIB-SEM Tribeam system (Thermo Fisher Scientific Helios 5 Laser Hydra UX).

4.4. Micro X-ray computed tomography

Slurry-casted NMC622 without laser processing and laser-structured NMC622 electrodes were secured on a petri dish with polyimide tape and fixed to the translation table of a laser micro-machining instrument (A Series, Oxford Lasers Ltd.) containing a 532 nm laser with a spot size of ca. 40 μm. The NMC622 electrodes were then successively milled to a rectangular tab with dimensions of ca. 1.5×4 mm^2 [63]. The obtained samples were scanned with a lab-based micro-CT instrument (Xradia Versa 520, Carl Zeiss Inc.), with an 80 kV tube voltage and 40X optical magnification. The voxel size is around 0.3 μm and the volume size is around $800\times800\times800$ mm^3. The radiographs were reconstructed in a 3D volume using a filtered back-projection algorithm implemented in the commercially available Zeiss XMReconstructor (Carl Zeiss Inc.) [64].

4.5. X-ray photoelectron spectroscopy (XPS) analysis

XPS Analysis was performed using a Kratos Axis SUPRA XPS fitted with a monochromated Al kα X-ray source (1486.7 eV), a spherical sector analyser and 3 multichannel resistive plate, 128 channel delay line detectors. All data were recorded at 150 W and a spot size of 700×300 μm. Survey scans were recorded at a pass energy of 160 eV, and high-resolution scans were recorded at a pass energy of 20 eV. Electronic charge neutralization was achieved using a magnetic immersion lens. Filament current = 0.27 A, charge balance = 3.3 V, filament bias = 3.8 V. All sample data were recorded at a pressure below

10–8 Torr and at 150 K temperature. Data were analysed using CasaXPS v2.3.20PR1.0 and the spectra were calibrated with C1s peak at 284.8 eV.

4.6. Electrolyte wetting measurement

All NMC622 electrodes were cut into circular with a diameter of 14.8 mm. An identical volume of ~8 μL of electrolyte (1 M LiPF6 in EC:EMC 3:7 v/v + VC 2 wt% (PuriEL)) was dropped on the top of NMC622 electrodes on a contact angle goniometer (Ossila) and the process was recorded by a high-speed camera.

4.7. Coin cell assembly

2032-type half-cell and full-cell coin cells were constructed for electrochemical tests. Slurry-casted and laser-structured NMC622 electrodes with a diameter of 14.8 mm serve as the cathodes. A tri-layer 2325 separator with a diameter of 16 mm (Celgard) and 100 μL electrolyte of 1 M LiPF6 in EC:EMC 3:7 v/v + VC 2 wt% (PuriEL) were used. Li-metal disc and graphite electrode with a diameter of 15 mm were used as anodes in half cells and full cells, respectively. After the assembly of coin cells, a formation step composed of two charge–discharge cycles at a $10\ \mathrm{mA\ g^{-1}}$ was conducted within a voltage window of 2.5 to 4.25 V vs. Li/Li$^+$ for NMC622 half-cells using a BCS-805 Biologic battery cycler (Biologic, France).

4.8. Cyclic voltammetry

Cyclic voltammetry was performed at different scan rates of 0.05, 0.06, 0.07, 0.08, 0.09 and $0.1\ \mathrm{mV}\ s^{-1}$ at a voltage window of 2.5–4.25 V using a BCS-805 Biologic battery cycler (Biologic, France).

4.9. Electrochemical impedance spectroscopy

Electrochemical impedance spectroscopy (PEIS) was performed with a VMP3 potentiostat at a state of charge (SOC) of 50 %. A frequency range of 10 mHz to 1 MHz (with 7 points per decade readings) was applied with a 10 mV amplitude. For the data analysis, EC-Lab software was used for the equivalent circuit model fitting.

4.10. Galvanostatic intermittent titration technique

Galvanostatic intermittent titration technique (GITT) was performed by charging and discharging NMC622 half cells with applied identical pulses at C/10 for 15 mins and followed by a relaxation period of 3 h. The diffusion coefficient, D, was calculated by a modified equation [65] based on Weppner and Huggins's work [66].

$$D = \frac{4}{\pi\tau}\left(\frac{n_m V_m}{S}\right)^2\left(\frac{\Delta E_s}{\Delta E_t}\right)^2$$

Where τ is the pulse duration, n_m is the number of moles, V_m is the molar volume, S is the contact area between the electrode and electrolyte, ΔE_s is the linear voltage change when a pulse is applied, ΔE_t is the change in the steady-state voltages during the relaxation period. Both the molar volume and contact area are estimated by assuming that active material particles are perfectly spherical with a radius of 10 μm. The instantaneous voltage change is defined as the IR drop which comprises two parts: ohmic overpotential (η_{ohm}) and charge-transfer overpotential (η_{CT}). Therefore, the charge-transfer overpotential (η_{CT}) can be calculated by

$$\eta_{CT} = IR\ drop - \eta_{ohm}$$

The ohmic overpotential (η_{ohm}) can be calculated by the ohmic resistance (~2.5 Ω measured by EIS in this work) multiplied by the applied current, I. The exchange current density, I_0, and charge transfer resistance, R_{CT}, can be calculated by

$$I_0 S = \frac{RT}{F}\frac{I}{\eta_{CT}}$$

$$R_{CT} = \frac{RT}{I_0 F}$$

Where R is the gas constant ($8.314\ \mathrm{J\ mol^{-1}\ K^{-1}}$), T is the temperature (298.15 K), F is the Faraday constant ($9.65\times10^4\ \mathrm{C\ mol^{-1}}$). More details can be found in [52].

4.11. Rate testing

NMC622 half cells were charged and discharged at different current densities of 10, 20, 50, 100, 200, 400, 600, 800, 1000 and 10 mA/g for five cycles at each current density within a voltage window of 2.5 to 4.25 V vs. Li/Li$^+$, using a BCS-805 Biologic battery cycler (Biologic, France). For charging, constant current-constant voltage (CC—CV) charging was employed with constant current densities of 10–1000 mA/g and, a current limit was set as one-tenth of the constant current at a constant voltage of 4.25 V.

4.12. Cycling testing

NMC622 half cells and full cells were charged and discharged firstly at 10 mA/g for two cycles and then at 100 mA/g for 500 cycles, within a voltage window of 2.5 to 4.25 V vs. Li/Li$^+$, using a BCS-805 Biologic battery cycler (Biologic, France). The same CC—CV charging as described in the section of Rate Testing was used.

4.13. X-ray CT image processing and electrochemical modelling

The raw CT images were processed using Avizo image analysis software (Avizo, Thermo Fisher Scientific, Waltham, Massachusetts, U. S.). A gaussian filter was applied to both images, which provided a smoother domain for meshing, then the volume of interest (see Figs. 5a and b was extracted. Ilastik, a machine learning-based, open-source segmentation software (Berg et al. [67], was used to segment the filtered image. Finally, Simpleware ScaniP was used to mesh the segmented images, giving approximately 3.1 and 4.3 million linear tetrahedral elements for structured and unstructured electrodes respectively. The model is based on a single electrode (half-cell).

The model framework and parameters, as outlined in Boyce et al. [59], were implemented in the finite element software COMSOL Multiphysics (v6.1, Sweden). We include a summary of the model framework and material parameters in Supplementary Information Table 1, 2, 3, 4. The Parallel Direct Sparse Solver (PARDISO) was used to solve the discretised transport and electrode kinetics equations. A segregated approach was taken, which involved solving the coupled field variables in a sequential, staggered way. Time stepping was handled using 2nd order backward Euler differentiation. The electrodes were discharged at 20, 50, 100, 200 and $400\ \mathrm{mA\ g^{-1}}$ to match the experiments.

CRediT authorship contribution statement

Pengcheng Zhu: Writing – review & editing, Writing – original draft, Methodology, Investigation, Formal analysis, Data curation, Conceptualization. **Adam Boyce:** Writing – review & editing, Software, Investigation, Formal analysis. **Sohrab R. Daemi:** Investigation, Data curation. **Bo Dong:** Methodology, Formal analysis. **Yongxiu Chen:** Methodology, Formal analysis. **Shaoliang Guan:** Writing – original draft, Methodology, Formal analysis. **Mickey Crozier:** Resources, Methodology. **Yu-Lung Chiu:** Resources, Methodology. **Alison J. Davenport:** Writing – original draft, Investigation, Formal analysis. **Rhodri Jervis:** Resources, Methodology. **Paul Shearing:** Resources, Methodology. **Reza N. Esfahani:** Writing – review & editing, Supervision, Methodology, Investigation, Conceptualization. **Peter R. Slater:**

Methodology, Investigation, Funding acquisition, Project administration, Supervision, Writing – original draft, Writing – review & editing. **Emma Kendrick:** Conceptualization, Formal analysis, Investigation, Methodology, Project administration, Resources, Supervision, Writing – review & editing.

Declaration of competing interest

The authors declare that they have no known competing financial interests or personal relationships that could have appeared to influence the work reported in this paper.

Data availability

Data will be made available on request.

Acknowledgements

Supplementary materials

Supplementary material associated with this article can be found, in the online version, at doi:10.1016/j.ensm.2024.103373.

References

[1] J.B. Goodenough, Electrochemical energy storage in a sustainable modern society, Energy Environ. Sci. 7 (2014) 14–18.
[2] S.J. Davis, N.S. Lewis, M. Shaner, S. Aggarwal, D. Arent, I.L. Azevedo, S.M. Benson, T. Bradley, J. Brouwer, Y.-M. Chiang, Net-zero emissions energy systems, Science 360 (2018) eaas9793.
[3] T. Beckford, G. Jackson-Johns, A. Daoud, G. Finn, T. Dowden, The Role of Hydrogen and Batteries in Delivering Net Zero in the UK by 2050, 2023.
[4] Y. Ding, Z.P. Cano, A. Yu, J. Lu, Z. Chen, Automotive Li-ion batteries: current status and future perspectives, Electrochem. Energy Rev. 2 (2019) 1–28.
[5] S. Sripad, V. Viswanathan, Performance metrics required of next-generation batteries to make a practical electric semi truck, ACS Energy Lett. 2 (2017) 1669–1673.
[6] F. Zenith, Battery-powered freight trains, Nat. Energy 6 (2021) 1003–1004.
[7] V. Viswanathan, A.H. Epstein, Y.-M. Chiang, E. Takeuchi, M. Bradley, J. Langford, M. Winter, The challenges and opportunities of battery-powered flight, Nature 601 (2022) 519–525.
[8] J.B. Goodenough, How we made the Li-ion rechargeable battery, Nat. Electron. 1 (2018) 204.
[9] A. Manthiram, A reflection on lithium-ion battery cathode chemistry, Nat. Commun. 11 (2020) 1550.
[10] A. Manthiram, An outlook on lithium ion battery technology, ACS Cent. Sci. 3 (2017) 1063–1069.
[11] Y. Lakhdar, H. Geary, M. Houck, D. Gastol, A.S. Groombridge, P.R. Slater, E. Kendrick, Optimization of electrode and cell design for ultrafast-charging lithium-ion batteries based on molybdenum niobium oxide anodes, ACS Appl. Energy Mater. 5 (2022) 11229–11240.
[12] Y. Lakhdar, Y. Chen, H. Geary, M.E. Houck, A.S. Groombridge, P.R. Slater, E. Kendrick, Toward higher-power Li-ion batteries: unravelling kinetics and thermodynamics of MoNb12O33 vs. NMC622, J. Power Sources 588 (2023) 233710.
[13] L. Zhou, K. Zhang, Z. Hu, Z. Tao, L. Mai, Y.M. Kang, S.L. Chou, J. Chen, Recent developments on and prospects for electrode materials with hierarchical structures for lithium-ion batteries, Adv. Energy Mater. 8 (2018) 1701415.
[14] A. Vu, Y. Qian, A. Stein, Porous electrode materials for lithium-ion batteries–how to prepare them and what makes them special, Adv. Energy Mater. 2 (2012) 1056–1085.
[15] J. Ye, A.C. Baumgaertel, Y.M. Wang, J. Biener, M.M. Biener, Structural optimization of 3D porous electrodes for high-rate performance lithium ion batteries, ACS Nano 9 (2015) 2194–2202.
[16] J. Ni, L. Li, Cathode architectures for rechargeable ion batteries: progress and perspectives, Adv. Mater. 32 (2020) 2000288.
[17] P. Zhu, P.R. Slater, E. Kendrick, Insights into architecture, design and manufacture of electrodes for Lithium-ion batteries, Mater. Des. (2022) 111208.
[18] Y. Kuang, C. Chen, D. Kirsch, L. Hu, Thick electrode batteries: principles, opportunities, and challenges, Adv. Energy Mater. 9 (2019) 1901457.
[19] Z. Du, D.L. Wood, C. Daniel, S. Kalnaus, J. Li, Understanding limiting factors in thick electrode performance as applied to high energy density Li-ion batteries, J. Appl. Electrochem. 47 (2017) 405–415.
[20] J. Li, Z. Du, R.E. Ruther, S.J. An, L.A. David, K. Hays, M. Wood, N.D. Phillip, Y. Sheng, C. Mao, Toward low-cost, high-energy density, and high-power density lithium-ion batteries, JOM 69 (2017) 1484–1496.
[21] H. Zhao, Q. Yang, N. Yuca, M. Ling, K. Higa, V.S. Battaglia, D.Y. Parkinson, V. Srinivasan, G. Liu, A convenient and versatile method to control the electrode microstructure toward high-energy lithium-ion batteries, Nano Lett. 16 (2016) 4686–4690.
[22] W. Deng, W. Shi, Q. Liu, J. Jiang, X. Li, X. Feng, Constructing gradient porous structure in thick Li4Ti5O12 electrode for high-energy and stable lithium-ion batteries, ACS Sustain. Chem. Eng 8 (2020) 17062–17068.
[23] L.L. Lu, Y.Y. Lu, Z.J. Xiao, T.W. Zhang, F. Zhou, T. Ma, Y. Ni, H.B. Yao, S.H. Yu, Y. Cui, Wood-inspired high-performance ultrathick bulk battery electrodes, Adv. Mater. 30 (2018) 1706745.
[24] C. Chen, S. Xu, Y. Kuang, W. Gan, J. Song, G. Chen, G. Pastel, B. Liu, Y. Li, H. Huang, Nature-Inspired Tri-Pathway Design Enabling High-Performance Flexible Li–O2 Batteries, Adv. Energy Mater. 9 (2019) 1802964.
[25] C. Huang, M. Dontigny, K. Zaghib, P.S. Grant, Low-tortuosity and graded lithium ion battery cathodes by ice templating, J. Mater. Chem. A 7 (2019) 21421–21431.
[26] S.H. Lee, A. Mahadevegowda, C. Huang, J.D. Evans, P.S. Grant, Spray printing of self-assembled porous structures for high power battery electrodes, J. Mater. Chem. A 6 (2018) 13133–13141.
[27] D. Gastol, M. Capener, C. Reynolds, C. Constable, E. Kendrick, Microstructural design of printed graphite electrodes for lithium-ion batteries, Mater. Des. 205 (2021) 109720.
[28] J. Li, M.C. Leu, R. Panat, J. Park, A hybrid three-dimensionally structured electrode for lithium-ion batteries via 3D printing, Mater. Des. 119 (2017) 417–424.
[29] S. Park, B. Shi, Y. Shang, K. Deng, K. Fu, Structured electrode additive manufacturing for lithium-ion batteries, Nano Lett. 22 (2022) 9462–9469.
[30] K.-H. Chen, M.J. Namkoong, V. Goel, C. Yang, S. Kazemiabnavi, S. Mortuza, E. Kazyak, J. Mazumder, K. Thornton, J. Sakamoto, Efficient fast-charging of lithium-ion batteries enabled by laser-patterned three-dimensional graphite anode architectures, J. Power Sources 471 (2020) 228475.
[31] J. Park, C. Jeon, W. Kim, S.-J. Bong, S. Jeong, H.-J. Kim, Challenges, laser processing and electrochemical characteristics on application of ultra-thick electrode for high-energy lithium-ion battery, J. Power Sources 482 (2021) 228948.
[32] S. Kalnaus, K. Livingston, W.B. Hawley, H. Wang, J. Li, Design and processing for high performance Li ion battery electrodes with double-layer structure, J. Energy Storage 44 (2021) 103582.
[33] R. Diehm, J. Kumberg, C. Dörrer, M. Müller, W. Bauer, P. Scharfer, W. Schabel, In situ investigations of simultaneous two-layer slot die coating of component-graded anodes for improved high-energy Li-ion batteries, Energy Technol. 8 (2020) 1901251.
[34] J. Li, J. Fleetwood, W.B. Hawley, W. Kays, From materials to cell: state-of-the-art and prospective technologies for lithium-ion battery electrode processing, Chem. Rev. 122 (2021) 903–956.
[35] W. Pfleging, A review of laser electrode processing for development and manufacturing of lithium-ion batteries, Nanophotonics 7 (2018) 549–573.
[36] J. Sandherr, S. Nester, M.-J. Kleefoot, M. Bolsinger, C. Weisenberger, A. Haghipour, D.K. Harrison, S. Ruck, H. Riegel, V. Knoblauch, Improving the ionic transport properties of graphite anodes for lithium ion batteries by surface modification using nanosecond laser, J. Power Sources 549 (2022) 232077.
[37] J.S. Kim, W. Pfleging, R. Kohler, H.J. Seifert, T.Y. Kim, D. Byun, H.-G. Jung, W. Choi, J.K. Lee, Three-dimensional silicon/carbon core–shell electrode as an anode material for lithium-ion batteries, J. Power Sources 279 (2015) 13–20.
[38] Y. Zheng, H. Seifert, H. Shi, Y. Zhang, C. Kübel, W. Pfleging, 3D silicon/graphite composite electrodes for high-energy lithium-ion batteries, Electrochim. Acta 317 (2019) 502–508.
[39] P. Zhu, H.J. Seifert, W. Pfleging, The ultrafast laser ablation of Li (Ni0. 6Mn0. 2Co0. 2) o2 electrodes with high mass loading, Appl. Sci. 9 (2019) 4067.
[40] J. Park, H. Song, I. Jang, J. Lee, J. Um, S.-g. Bae, J. Kim, S. Jeong, H.-J. Kim, Three-dimensionalization via control of laser-structuring parameters for high energy and high power lithium-ion battery under various operating conditions, J. Energy Chem. 64 (2022) 93–102.
[41] P. Smyrek, J. Pröll, H. Seifert, W. Pfleging, Laser-induced breakdown spectroscopy of laser-structured Li (NiMnCo) O2 electrodes for lithium-ion batteries, J. Electrochem. Soc. 163 (2015) A19.
[42] A. Davoodabadi, J. Li, Y. Liang, R. Wang, H. Zhou, D.L. Wood, T.J. Singler, C. Jin, Characterization of surface free energy of composite electrodes for lithium-ion batteries, J. Electrochem. Soc. 165 (2018) A2493.

[43] A. Davoodabadi, J. Li, Y. Liang, D.L. Wood III, T.J. Singler, C. Jin, Analysis of electrolyte imbibition through lithium-ion battery electrodes, J. Power Sources 424 (2019) 193–203.

[44] A. Davoodabadi, J. Li, H. Zhou, D.L. Wood III, T.J. Singler, C. Jin, Effect of calendering and temperature on electrolyte wetting in lithium-ion battery electrodes, J. Energy Storage 26 (2019) 101034.

[45] A. Furlan, J. Lu, L. Hultman, U. Jansson, M. Magnuson, Crystallization characteristics and chemical bonding properties of nickel carbide thin film nanocomposites, J. Phys. 26 (2014) 415501.

[46] E. Björklund, D. Brandell, M. Hahlin, K. Edström, R. Younesi, How the negative electrode influences interfacial and electrochemical properties of LiNi1/3Co1/3Mn1/3O2 cathodes in Li-ion batteries, J. Electrochem. Soc. 164 (2017) A3054.

[47] N.D. Phillip, C. Daniel, G.M. Veith, Influence of binder coverage on interfacial chemistry of thin film LiNi0. 6Mn0. 2Co0. 2O2 cathodes, J. Electrochem. Soc. 167 (2020) 040521.

[48] P. Zhu, Y. Zhao, Cyclic voltammetry measurements of electroactive surface area of porous nickel: peak current and peak charge methods and diffusion layer effect, Mater. Chem. Phys. 233 (2019) 60–67.

[49] C. Brett, A.M.O. Brett, Electrochemistry: principles, methods, and applications, (No Title) (1993).

[50] K. Tang, X. Yu, J. Sun, H. Li, X. Huang, Kinetic analysis on LiFePO4 thin films by CV, GITT, and EIS, Electrochim. Acta 56 (2011) 4869–4875.

[51] J. Liu, J. Wang, C. Xu, H. Jiang, C. Li, L. Zhang, J. Lin, Z.X. Shen, Advanced energy storage devices: basic principles, analytical methods, and rational materials design, Adv. Sci. 5 (2018) 1700322.

[52] Y. Chen, J. Key, K. O'regan, T. Song, Y. Han, E. Kendrick, Revealing the rate-limiting electrode of lithium batteries at high rates and mass loadings, Chem. Eng. J. 450 (2022) 138275.

[53] T.E. Ashton, P.J. Baker, C. Sotelo-Vazquez, C.J. Footer, K.M. Kojima, T. Matsukawa, T. Kamiyama, J.A. Darr, Stoichiometrically driven disorder and local diffusion in NMC cathodes, J. Mater. Chem. A 9 (2021) 10477–10486.

[54] H. Gao, Q. Wu, Y. Hu, J.P. Zheng, K. Amine, Z. Chen, Revealing the rate-limiting Li-ion diffusion pathway in ultrathick electrodes for Li-ion batteries, J. Phys. Chem. Lett. 9 (2018) 5100–5104.

[55] A. Nickol, T. Schied, C. Heubner, M. Schneider, A. Michaelis, M. Bobeth, G. Cuniberti, GITT analysis of lithium insertion cathodes for determining the lithium diffusion coefficient at low temperature: challenges and pitfalls, J. Electrochem. Soc. 167 (2020) 090546.

[56] M. Gaberšček, Understanding Li-based battery materials via electrochemical impedance spectroscopy, Nat. Commun. 12 (2021) 6513.

[57] A.R. Bredar, A.L. Chown, A.R. Burton, B.H. Farnum, Electrochemical impedance spectroscopy of metal oxide electrodes for energy applications, ACS Appl. Energy Mater. 3 (2020) 66–98.

[58] N. Meddings, M. Heinrich, F. Overney, J.-S. Lee, V. Ruiz, E. Napolitano, S. Seitz, G. Hinds, R. Raccichini, M. Gaberšček, Application of electrochemical impedance spectroscopy to commercial Li-ion cells: a review, J. Power Sources 480 (2020) 228742.

[59] A.M. Boyce, X. Lu, D.J. Brett, P.R. Shearing, Exploring the influence of porosity and thickness on lithium-ion battery electrodes using an image-based model, J. Power Sources 542 (2022) 231779.

[60] X. Lu, A. Bertei, D.P. Finegan, C. Tan, S.R. Daemi, J.S. Weaving, K.B. O'Regan, T. M. Heenan, G. Hinds, E. Kendrick, 3D microstructure design of lithium-ion battery electrodes assisted by X-ray nano-computed tomography and modelling, Nat. Commun. 11 (2020) 1–13.

[61] J. Ma, J. Sung, J. Hong, S. Chae, N. Kim, S.-H. Choi, G. Nam, Y. Son, S.Y. Kim, M. Ko, Towards maximized volumetric capacity via pore-coordinated design for large-volume-change lithium-ion battery anodes, Nat. Commun. 10 (2019) 475.

[62] W. Zhou, J. Chen, X. Xu, X. Han, M. Chen, L. Yang, S.-i. Hirano, Large areal capacity all-in-one lithium-ion battery based on boron-doped silicon/carbon hybrid anode material and cellulose framework, J Colloid Interface Sci 612 (2022) 679–688.

[63] C. Tan, S. Daemi, T. Heenan, F. Iacoviello, A. Leach, L. Rasha, R. Jervis, D. Brett, P. Shearing, Rapid preparation of geometrically optimal battery electrode samples for nano scale X-ray characterisation, J. Electrochem. Soc. 167 (2020) 060512.

[64] J. Bailey, T. Heenan, D. Finegan, X. Lu, S. Daemi, F. Iacoviello, N. Backeberg, O. Taiwo, D. Brett, A. Atkinson, Laser-preparation of geometrically optimised samples for X-ray nano-CT, J Microsc 267 (2017) 384–396.

[65] C.-H. Chen, F.B. Planella, K. O'regan, D. Gastol, W.D. Widanage, E. Kendrick, Development of experimental techniques for parameterization of multi-scale lithium-ion battery models, J. Electrochem. Soc. 167 (2020) 080534.

[66] W. Weppner, R.A. Huggins, Determination of the kinetic parameters of mixed-conducting electrodes and application to the system Li3Sb, J. Electrochem. Soc. 124 (1977) 1569.

[67] S. Berg, D. Kutra, T. Kroeger, C.N. Straehle, B.X. Kausler, C. Haubold, M. Schiegg, J. Ales, T. Beier, M. Rudy, Ilastik: interactive machine learning for (bio) image analysis, Nat. Methods 16 (2019) 1226–1232.